On the Decadal Variability of the Eddy Kinetic Energy in the Kuroshio Extension

YANG YANG

School of Atmospheric Sciences, Nanjing University of Information Science and Technology, Nanjing, China

X. SAN LIANG

School of Marine Sciences, and School of Atmospheric Sciences, Nanjing University of Information Science and Technology, Nanjing, China

BO QIU AND SHUIMING CHEN

Department of Oceanography, University of Hawai'i at Mānoa, Honolulu, Hawaii

(Manuscript received 29 August 2016, in final form 4 March 2017)

ABSTRACT

Previous studies have found that the decadal variability of eddy kinetic energy (EKE) in the upstream Kuroshio Extension is negatively correlated with the jet strength, which seems counterintuitive at first glance because linear stability analysis usually suggests that a stronger jet would favor baroclinic instability and thus lead to stronger eddy activities. Using a time-varying energetics diagnostic methodology, namely, the localized multiscale energy and vorticity analysis (MS-EVA), and the MS-EVA-based nonlinear instability theory, this study investigates the physical mechanism responsible for such variations with the state estimate from the Estimating the Circulation and Climate of the Ocean (ECCO), Phase II. For the first time, it is found that the decadal modulation of EKE is mainly controlled by the barotropic instability of the background flow. During the high-EKE state, violent meanderings efficiently induce strong barotropic energy transfer from mean kinetic energy (MKE) to EKE despite the rather weak jet strength. The reverse is true in the low-EKE state. Although the enhanced meander in the high-EKE state also transfers a significant portion of energy from mean available potential energy (MAPE) to eddy available potential energy (EAPE) through baroclinic instability, the EAPE is not efficiently converted to EKE as the two processes are not well correlated at low frequencies revealed in the time-varying energetics. The decadal modulation of barotropic instability is found to be in pace with the North Pacific Gyre Oscillation but with a time lag of approximately 2 years.

1. Introduction

The Kuroshio Extension has been recognized as a highly variable frontal jet characterized with large-amplitude meanders and vigorous mesoscale eddies (Fig. 1; Mizuno and White 1983). The meandering jet and its associated eddies have been found to influence local fisheries and marine ecosystems by affecting the regional distribution of heat and nutrients (Miller et al. 2004; Nishikawa and Yasuda 2011; Sasai et al. 2010; Chiba et al. 2013) and leave significant imprints on the local as well as basin-scale climate in the North Pacific through strong air–sea interactions (Latif and Barnett 1994; Schneider et al. 2002; Qiu et al. 2014; Wang and Liu 2015). With such broad impacts, the Kuroshio Extension has become an important area of interdisciplinary research for decades (Kida et al. 2015).

Significant decadal variability has been observed in the Kuroshio Extension, reflected by multiple indices such as the regional sea surface height (SSH) anomalies, jet strength, latitudinal position, and pathlength, to name a few (Qiu and Chen 2005). During the past decade, continuing efforts have been made to understand the dynamics behind this low-frequency variability. Generally, the decadal variability could be either driven by external forcing or due to internal dynamics. Contribution from external forcing is considered to be more important by previous studies considering the Kuroshio

Corresponding author: X. San Liang, sanliang@courant.nyu.edu

DOI: 10.1175/JPO-D-16-0201.1

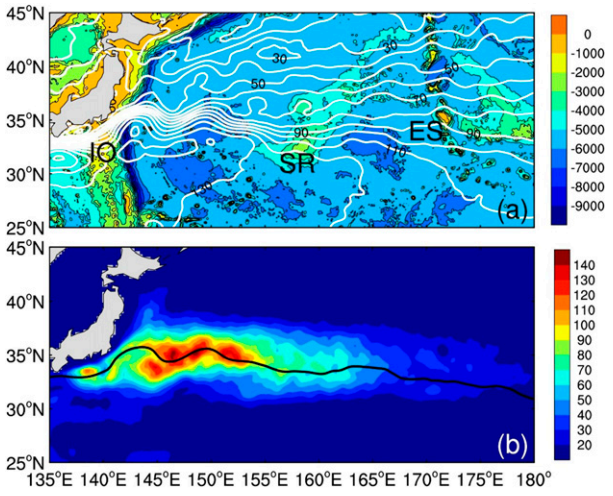

FIG. 1. (a) Sea surface height based on the AVISO data (white contours; cm) and bathymetry (colored shading; m) in the western North Pacific. Labeled in the figure are Izu–Ogasawara Ridge (IO), Shatsky Rise (SR), and Emperor Seamounts (ES). (b) Long-term mean eddy kinetic energy (colored shading; J m^{-3}). The black line shows the jet axis (100-cm isobath of the sea surface height).

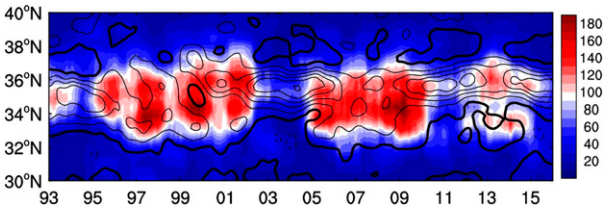

FIG. 2. Time_latitude diagram of the observed EKE (colored shading; J m^{-3}) and eastward surface geostrophic velocity (black contours; cm s^{-1}) averaged over 142°–150°E. Thick black contours denote $u_{geo} = 0$. Both time series are low_pass filtered with a yearly running mean.

Extension's linear response to the incoming westward propagation of large-scale baroclinic Rossby waves, which was forced by anomalous wind stress curl in the central North Pacific (Miller et al. 1998; Deser et al. 1999; Seager et al. 2001; Qiu 2003; Kwon and Deser 2007; Ceballos et al. 2009; Sasaki and Schneider 2011). On the other hand, the intrinsic mechanism claimed that the decadal variability is an internal mode of the highly nonlinear western boundary current (WBC) system, which is confirmed in a variety of numerical models ranging from idealized quasigeostrophic models to realistic ocean general circulation models (OGCMs; McCalpin and Haidvogel 1996; Simonnet and Dijkstra 2002; Hogg et al. 2005; Nonaka et al. 2006; Berloff et al. 2007; Primeau and Newman 2008; Pierini et al. 2009). Internal processes, such as instabilities and eddy–mean flow interactions, whether they are self-sustained or modulated by external forcing, are indispensable ingredients to achieve a full understanding of the dynamics underlying the decadal variability in this region.

Baroclinic instability has been recognized as the primary source of eddy kinetic energy (EKE) in the global ocean (Gill et al. 1974; Ferrari and Wunsch 2009; von Storch et al. 2012). Mesoscale eddies derive much of their energy from the available potential energy (APE) of the large-scale mean flow (Pedlosky 1987). Hence, it is generally expected that the eddy activity in WBCs should be stronger when the mean flow is more baroclinic. Recent studies based on satellite observations and numerical simulations have reported that the low-frequency (interannual to decadal) changes of EKE in several ocean sectors are indeed controlled by baroclinic instability of the background currents, for example, the North Atlantic Ocean (Penduff et al. 2004), the southeast Indian Ocean (Jia et al. 2011), the Azores Current (Volkov and Fu 2011), the western North Pacific Subtropical Gyre (Qiu and Chen 2013), and the northeastern South China Sea (Sun et al. 2016). Unlike those regions where the low-frequency EKE variability is largely in phase with the baroclinicity of the background flow, the Kuroshio Extension appears not. Figure 2 shows the temporal variations of EKE and eastward geostrophic velocity as a function of latitude and time averaged between 142° and 150°E. Elevated EKE level is detected during years when the background jet is weak and meridionally broad (i.e., 1996–2001, 2005–09, and 2013–14), whereas reduced EKE is observed during the years when the mean flow is strong and narrow (i.e., 1993–95, 2002–05, and 2009–12). This robust inverse relationship between the EKE and the jet strength in the upstream Kuroshio Extension, as first noted by Qiu and Chen (2005), seems rather counterintuitive at first glance, since linear stability analysis usually suggests that a stronger jet would favor baroclinic instability and thus result in more eddy generation. Considering this, Qiu and Chen (2005) argued that baroclinic instability is not the possible mechanism controlling the decadal modulation of the observed mesoscale eddy field in this region. Instead, they suggested that there exists a possible interaction between the decadally migrating jet and the meridionally aligned Izu–Ogasawara Ridge. When the incoming negative SSH anomalies generated from the central North Pacific reach the upstream Kuroshio Extension, the inflow jet off Japan tends to shift southward and run into a shallow portion of the ridge, leading to the growth of unstable perturbations. In contrast, when the jet tends to take a northward path because of the positive incoming SSH anomalies from the east, it flows over a deep channel of the ridge, resulting in a relatively stable jet. The recent study by Bishop (2013) analyzed 16-month observational records from the Kuroshio Extension System Study (KESS) and reported that the

vertical coupling between the deep eddies and the upper jet is consistent with a baroclinic instability scenario after the regime shifts from a stable state to an unstable state. Up to now, we are unware of any other studies focusing on the mechanism that gives rise to this peculiar decadal EKE variability in the upstream Kuroshio Extension. Questions like, but not limited to, the following are still to be addressed. Since it is found that the eddy activities are negatively correlated to the jet strength, which by the linear instability theory is correlated to the strength of baroclinic instability, one naturally wants to know whether indeed baroclinic instability is reduced when eddy activities are strong. If so, then, what is the mechanism governing the eddy growth, and what processes are involved in the low-frequency eddy modulation?

In this study, we address these issues by analyzing the time-varying eddy energetics. A multiscale energetics study in the time-varying sense is a notorious challenge in geophysical fluid dynamics. A recent comprehensive investigation is referred to Liang (2016); in section 2, we will give a brief introduction of the part relevant to this study. Another difficulty for the analysis is the short temporal coverage of in situ observation (e.g., KESS), while the information obtained from satellite altimetry is merely surface limited. We will hence use the available reanalysis data instead. Based on an eddy-resolving global hindcast model, the long-term climatology of the multiscale energetics in the Kuroshio Extension was recently addressed by Yang and Liang (2016). They found that the baroclinic energy pathway, transferring mean APE (MAPE) to eddy APE (EAPE) and finally converting to EKE, together with the barotropic energy pathway, transferring mean kinetic energy (MKE) to EKE, are equally important for the growth of the EKE in the upstream region of Kuroshio Extension. However, the energetics they examined is in a statistical mean sense; no time variation was considered. Although, as suggested by previous studies (Qiu and Chen 2005) that the baroclinic pathway can be potentially ruled out for the decadal changes in mesoscale eddy variability in this region, this first-guess argument has not considered the fact that the Kuroshio Extension, especially the upstream portion of it, is significantly nonzonal. Several studies have reported even weak nonzonal currents can lead to strong instabilities (e.g., Spall 2000; Smith 2007). The nonzonal component of the jet, as manifested by its meanderings, has been recognized to induce significant energy transfer from the mean flow to the eddies through efficient barotropic and baroclinic instability (Abernathey and Cessi 2014; Bischoff and Thompson 2014; Chapman et al. 2015; Chen et al. 2015; Elipot and Beal 2015). Thus, quantifying baroclinic instability and barotropic instability from the data is the key to uncovering the underlying dynamics of the decadal EKE modulation in the Kuroshio Extension system. Recently, Liang and Robinson (2005, 2007) developed a localized, finite-amplitude instability analysis, which is based on the localized multiscale energy and vorticity analysis (MS-EVA); it proves to be very efficient in diagnosing the nonlinear eddy–mean flow interactions and multiscale instabilities in real oceanic and atmospheric processes (Liang and Robinson 2009; Yang and Liang 2016). In the formalism, contributions from baroclinic and barotropic instabilities to the eddy energy generation as well as other sources, sinks, and redistributions of eddy energy can be explicitly computed. In this study, we will apply MS-EVA and the MS-EVA-based finite-amplitude hydrodynamic instability theory to investigate the instabilities and energetics associated with the decadal EKE modulation in the upstream Kuroshio Extension. The rest of the paper is organized as follows: We briefly introduce the MS-EVA in section 2 and the data description and validation in section 3. The major results are presented in section 4. They are then discussed and summarized in section 5.

2. Methodology

Ever since the Lorenz (1955) energy cycle was introduced in the atmosphere science, energetics analysis has become a powerful tool to diagnose the intrinsic and external energy sources and sinks and flow instabilities. Thus, it is natural to evaluate the decadal EKE variations in the Kuroshio Extension from the perspective of time-dependent energetics analysis, which, to our knowledge, has not been documented before [what Yang and Liang (2016) investigated is long-term mean energetics in this region]. In this section, we present a brief introduction of the localized MS-EVA and the MS-EVA-based theory of finite-amplitude baroclinic and barotropic instability; for details, see the references cited thereof.

Time-varying energetics analysis is a continuing challenge in geophysical fluid dynamics. Recently, Liang (2016) gave this a comprehensive review and elucidated the theoretical challenges and clarified some misconceptions currently in existence. In this study, we use the multiscale window transform (MWT) of Liang and Anderson (2007) to decompose the original fields into two orthogonal windows, namely, a low-frequency mean flow window and a high-frequency eddy window. To emphasize the contribution from the mesoscale eddy signals, the cutoff period of the window decomposition is set to 260 days,

which is consistent with the previous eddy characteristics studies of this region (Itoh and Yasuda 2010). We have tested the periods varying from 6 months to 2 years, and the results are all quantitatively similar. For easy reference, the mean flow window and the eddy window are denoted by $\varpi = 0, 1$, respectively. Within the MWT framework, the kinetic energy (KE) and APE on window ϖ are

$$K^{\varpi} = \frac{1}{2}\rho_0 \hat{\mathbf{u}}_H^{\sim\varpi} \cdot \hat{\mathbf{u}}_H^{\sim\varpi}, \quad \text{and} \tag{1}$$

$$A^{\varpi} = \frac{g^2}{2\rho_0 N^2}(\hat{\rho}^{\sim\varpi})^2, \tag{2}$$

respectively, where g is the acceleration due to gravity, $\mathbf{u}_H = (u, v)$ is the horizontal velocity vector, ρ_0 is the reference density, ρ is the density perturbation from the background profile $\overline{\rho}(z)$, $N = \sqrt{-g(\partial\overline{\rho}/\partial z)/\rho_0}$ is the buoyancy frequency, and $\widehat{(\cdot)}^{\sim\varpi}$ denotes MWT on window ϖ. A detailed derivation of the K^{ϖ} and A^{ϖ} equations are referred to Liang (2016); here, the results are summarized below:

$$\frac{\partial K^{\varpi}}{\partial t} + \underbrace{\nabla\cdot\left[\frac{1}{2}\rho_0\hat{\mathbf{u}}^{\sim\varpi}\widehat{(\mathbf{u}\mathbf{u}_H)}^{\sim\varpi}\right]}_{\nabla\cdot\mathbf{Q}_K^{\varpi}} = \underbrace{-\nabla\cdot(\hat{\mathbf{u}}^{\sim\varpi}\hat{p}^{\sim\varpi})}_{\nabla\cdot\mathbf{Q}_P^{\varpi}} \underbrace{-\left[\frac{1}{2}\rho_0(\hat{u}^{\sim\varpi})^2\nabla\cdot\mathbf{u}_u^{\varpi} + \frac{1}{2}\rho_0(\hat{v}^{\sim\varpi})^2\nabla\cdot\mathbf{u}_v^{\varpi}\right]}_{\Gamma_K^{\varpi}} + \underbrace{(-g\hat{\rho}^{\sim\varpi}\hat{w}^{\sim\varpi})}_{b^{\varpi}} + F_K^{\varpi}, \tag{3}$$

and

$$\frac{\partial A^{\varpi}}{\partial t} + \underbrace{\nabla\cdot\left[\frac{g^2}{2\rho_0 N^2}\hat{\rho}^{\sim\varpi}\widehat{(\rho\mathbf{u})}^{\sim\varpi}\right]}_{\nabla\cdot\mathbf{Q}_A^{\varpi}} = \underbrace{-A^{\varpi}\nabla\cdot\mathbf{u}_{\rho}^{\varpi}}_{\Gamma_A^{\varpi}} + \underbrace{g\hat{\rho}^{\sim\varpi}\hat{w}^{\sim\varpi}}_{-b^{\varpi}} + F_A^{\varpi}, \tag{4}$$

where $\mathbf{u} = (u, v, w)$ is the three-dimensional velocity vector, and p is the dynamic pressure. The terms $\mathbf{u}_u^{\varpi}$, $\mathbf{u}_v^{\varpi}$, and $\mathbf{u}_{\rho}^{\varpi}$ are referred to as the T-coupled velocity, which satisfies $\mathbf{u}_T^{\varpi} = \widehat{(\mathbf{u}T)}^{\sim\varpi}/\hat{T}^{\sim\varpi}$ for $T = u, v$, or ρ.

In (3) and (4), the Γ^{ϖ} terms represent the local process of cross-scale energy transfer to window ϖ. Recently, Liang (2016) proved that they actually can be written in a Lie bracket form, just like the Poisson bracket in Hamiltonian mechanics. The $\nabla\cdot\mathbf{Q}^{\varpi}$ terms denote the nonlocal process of energy flux divergence through advection or pressure work; positive (negative) values represent the energy transporting out of (into) the local domain. The b^{ϖ} term is the rate of buoyancy conversion connecting APE and KE. The external forcing and internal dissipation processes [denoted as F in (3) and (4)] are not explicitly calculated but considered as a residual in this study. Notice that the above terms in (3) and (4) are all four-dimensional field variables and so have all the localized information retained, which is essential for the diagnosis of the decadally varying eddy energetics in the Kuroshio Extension. Particularly, the transfer term Γ^{ϖ} has an interesting property, namely,

$$\sum_{\varpi}\sum_{n}\Gamma_n^{\varpi} = 0, \tag{5}$$

where $\sum_n$ is a summation over all the sampling time steps n [the subscript n is omitted through (1)–(4) for simplicity], and $\sum_{\varpi}$ is a summation over all scale windows ϖ [see Liang (2016) for details]. Notice that the transfer terms in the traditional formalism will sum to a divergence form that has zero global-mean values but nonzero local values. This makes the local interpretation of the cross-scale energy transfer process a difficult one since physically an energy transfer process should merely redistribute energy among scales (Rhines 1977; Cai et al. 2007; Liang and Robinson 2005). To distinguish, this process in the MS-EVA formalism is termed "canonical transfer." The canonical transfer is important in that they are closely related to the classical geophysical fluid dynamics (GFD) stability theory. Details can be found in Liang and Robinson (2007) and Liang (2016). In this study, we use the superscript $\varpi_0 \to \varpi_1$ to signify such window-to-window interactions and hence instabilities. Physically, a positive baroclinic (barotropic) transfer rate from the mean–flow window ($\varpi = 0$) to the eddy window ($\varpi = 1$) is indicative of baroclinic (barotropic) instability in the ocean. Figure 3 illustrates the energy diagram for a two-window decomposition.

3. Data description and validation

We use the model outputs from Estimating the Circulation and Climate of the Ocean (ECCO), Phase II (ECCO2) as the input of MS-EVA application. ECCO2

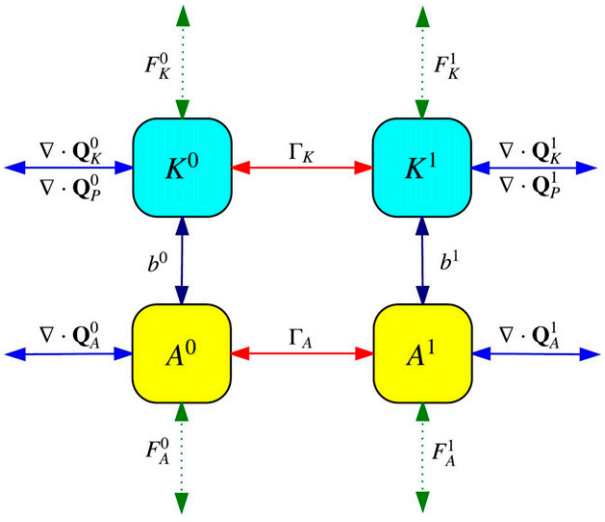

FIG. 3. Energy pathway diagram for a two-window decomposition. Red arrows indicate the energy transfer between the mean–flow (indicated as superscript 0) and eddy window (indicated as superscript 1), while navy arrows illustrate the buoyancy conversion connecting the KE and APE reservoirs. Blue dashed arrows indicate nonlocal processes transporting into or out of the local ocean domain. The forcing and dissipation processes are denoted as F terms (dashed green arrows).

is based on the Massachusetts Institute of Technology General Circulation Model (MITgcm; Marshall et al. 1997), which is a 3D, z-level, hydrostatic, Boussinesq ocean model, using cube sphere grid projection (cube92 version) with a mean horizontal resolution of 18 km. Vertically, the model has 50 levels, with resolution varying from 10 m near the sea surface to 456 m near the bottom at a maximum depth of 6150 m. The high-resolution global ocean state estimate is obtained by a least squares fit of the MITgcm to the available satellite and in situ data. Using a Green's function approach (Menemenlis et al. 2005), the least squares fit is employed for a number of control parameters (see the appendix for more information). With these optimized control parameters, the model is run forward freely, as in any ordinary model simulation. Since no data are taken in to interrupt the forward run, the state estimate is considered to be dynamically and kinematically consistent (Wunsch et al. 2009). Its high-resolution and decadal-long (1992–present) global output has been extensively used to examine the eddy dynamics and ocean energetics (Fu 2009; Zemskova et al. 2015; Chen et al. 2016). In this study, the 3-day-averaged dataset over 1993–2015 is used.

Simulating the phase evolution of frontal processes and the associated mesoscale eddy fields in the Kuroshio Extension region is a challenge because of the highly nonlinear and stochastic nature of the WBC system. In contrast, large-scale oceanic linear features, such as baroclinic Rossby waves, can be easily reproduced in numerical hindcast simulations (Qiu 2003; Taguchi et al. 2007). For instance, Taguchi et al. (2010) reported that salient features of decadal modulation of observed SSH in the Kuroshio Extension region are well captured in an eddy-resolving multidecadal ocean model hindcast simulation, while the modeled EKE in the upstream Kuroshio Extension region failed to reproduce the observed decadal phase evolution. We have tried some datasets and identified that the ECCO2 dataset is the one that has the decadal EKE variability appropriately simulated in this region (see the appendix). In the following, the SSH data from altimeter satellite products distributed by the Archiving, Validation, and Interpretation of Satellite Oceanographic (AVISO; Ducet et al. 2000) are used to test the degrees of fidelity of the ECCO2 state estimate in the Kuroshio Extension. Generally, the model has well reproduced the long-term mean surface circulation in the Kuroshio Extension (vectors in Figs. 4a,b). By conducting an empirical orthogonal function (EOF) analysis, we compare the dominant spatiotemporal mode of EKE obtained from the ECCO2 state estimate with that from the altimeters. During the period of 1993–2015, the first EOF mode accounts for 9.2% and 8.2% (reaches 34.4% and 31.4% after applying a 1-yr low-pass filter to the original EKE field) of the total EKE variance for the observation and the model, respectively. The EOF spatial pattern of the first mode from the model is similar to that from the altimetry (colored shades in Figs. 4a,b), both of which are characterized by a hot spot of variance in the first quasi-stationary meander region between 32° and 36°N and 141° and 147.5°E. The corresponding principle component (PC) from the model also captures the observed one favorably well, both of which show higher-than-normal variations in 1996–2001 and 2005–08 and lower-than-normal variations in 1993–95 and 2002–04. The linear correlation coefficient r between the two time series is 0.41 for the period during 1993–2008. The corresponding r between the two low-pass filtered series (with periods longer than 1 yr; not shown) reaches as high as 0.72 (statistically significant over the 95% confidence level). Notice that the model results are not well correlated with the observed one in some individual years such as 2009, 2011, and 2015. This discrepancy may result from multiple causes related to the model configurations, which is beyond the scope of the present study. To conclude this section, in Fig. 4 we plot the EKE time series averaged over the box of 32°–36°N and 142°–152°E (see the gray box in Fig. 4b), where the largest EKE variability occurs. This EKE time series is found to be dominated by its first EOF mode. The series

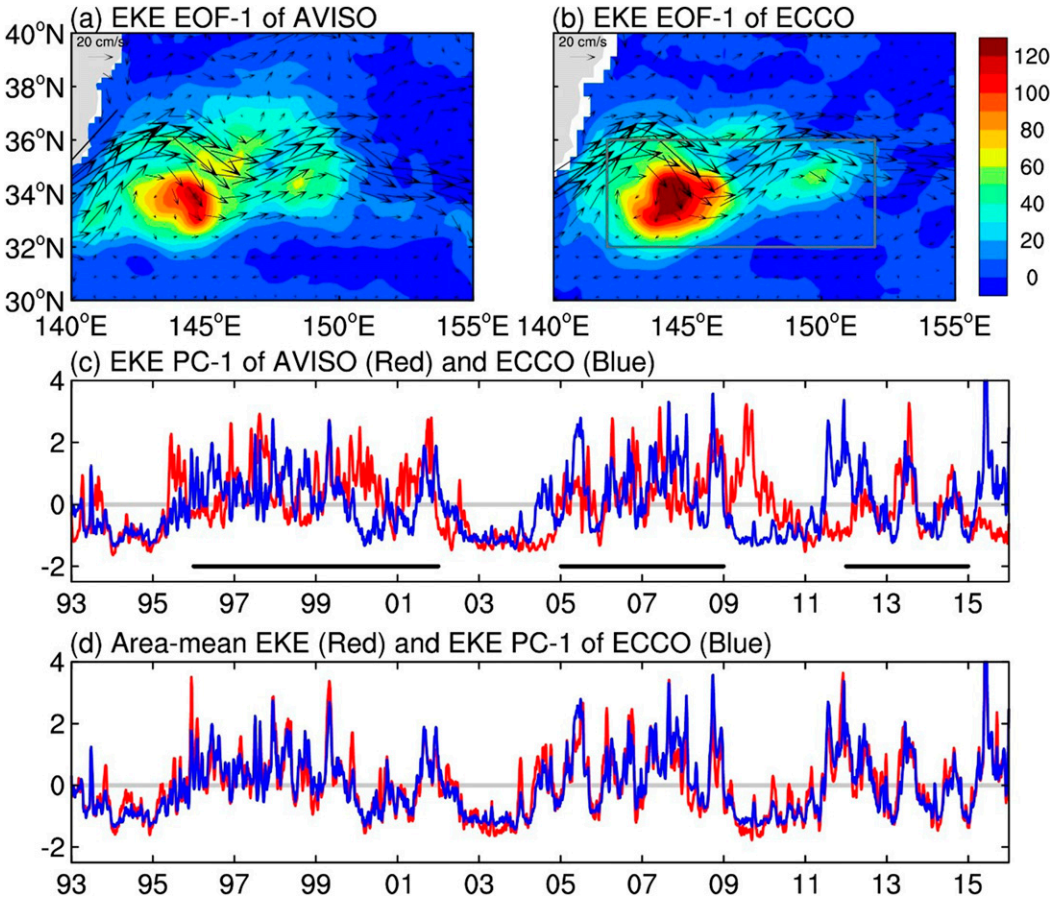

FIG. 4. First EOF mode of surface EKE from (a) the satellite observation and (b) ECCO2 state estimate. The spatial patterns (colored shading; J m^{-3}) are obtained by a regression of the EKE onto the normalized PCs of the EOF modes. The long-term mean of the surface geostrophic circulation (vectors; cm s^{-1}) is superposed in each map. The gray box represents the region with maximum EKE variance. (c) Normalized principal component (PC-1) of the observation (red) and ECCO2 state estimate (blue). The horizontal black lines indicate the periods when the Kuroshio Extension system is in the high-EKE state. (d) Normalized EKE time series averaged over the gray box of Fig. 4b (red), and the series of the first PC of the EKE (blue) from the ECCO2 state estimate.

almost coincides with the first PC series; the linear correlation coefficient between them is as high as 0.92. In other words, although the EKE variance explained by the first EOF mode is not so high, this mode effectively captures the regional coherent EKE variability. Particularly, the ECCO model successfully reproduced the two complete decadal cycles of the observed EKE. Thus, we can safely say that the model outputs are appropriate for the purpose of this study.

4. Results

To examine the spatial difference between the two dynamical states, composite maps are constructed. High-EKE and low-EKE states are defined based on the PC-1 of the simulated EKE (Fig. 4c). The high (low) phase occurs when the PC-1 series has a value greater (less) than 1 (−1) standard deviation. According to the definition above, 358 and 317 samples are selected for the high and low composites, respectively. The composite horizontal maps show that the high-EKE state is characterized by a spatially coherent strong EKE in the upstream Kuroshio Extension, while the EKE level reduces remarkably during the low-EKE state (color shades in Figs. 5a,b). To clarify the cause underlying the contrast between these bimodal states, it is helpful to examine the associated background circulation differences. The composite maps of the surface velocity field (vectors in Figs. 5a,b) capture the contrast in spatial patterns of the Kuroshio Extension jet and its associated southern recirculation gyre (SRG) between the two dynamic states. In the high-EKE state, the eastward-flowing jet appears broad and convoluted. During the low-EKE state, the eastward jet takes a straight path and

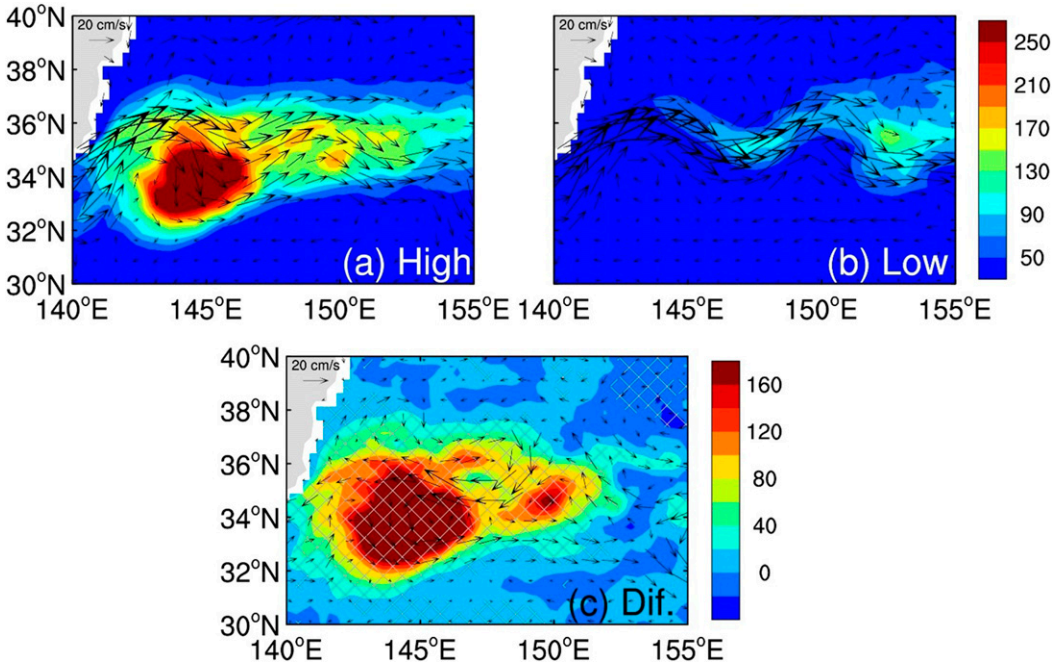

FIG. 5. Composite maps of the EKE (colored shading; J m^{-3}) and surface geostrophic circulation (vectors; cm s^{-1}) for (a) the high-EKE state and (b) the low-EKE state and (c) their difference in the ECCO2 state estimate. Hatched are regions where the corresponding differences are significant at the 95% confidence level.

is accompanied by a well-defined SRG south of the jet axis. The above description of the relationship between the background circulation state and the regional EKE in the ECCO2 state estimate is consistent with previous findings using altimetry observations (Qiu and Chen 2005, 2010), indicating again that the ECCO2 is reliable for the investigation of the decadal variability of the EKE in this region. The difference of the circulation between the two phases exhibits a train of anomalous cyclonic and anticyclonic circulations over the time-mean crest and trough (Fig. 5c), indicating that during the years when eddy activities are strong (weak), the Kuroshio Extension jet and its associated recirculation gyres are weak (strong), whereas the meanders are strong (weak). These results suggest that the decadal variability of EKE in this region is related to the stability of the jet's meanderings. In fact, the importance of stationary meanders in setting EKE distributions in the ocean has been reported in several recent studies. For instance, Abernathey and Cessi (2014) found that the standing meanders in the Southern Ocean are able to concentrate the eddy activity and meridional heat flux. Chapman et al. (2015) proposed that the oceanic storm tracks could be initiated in standing meanders where strong localized energy transfer from the mean field to the eddy field is found. Apart from bringing in elevated baroclinic instability, stationary meanders are also responsible for the sudden and strong positive transfer of KE from the mean flow to the eddies through barotropic instability (Elipot and Beal 2015).

To better reveal the cause of the decadal variation of the EKE in the upstream Kuroshio Extension, we employ the MS-EVA for the diagnostics. Generally, the EKE variability in an ocean domain can be influenced by direct local wind forcing, nonlinear energy transfers through barotropic and baroclinic instabilities, interactions between flow and topography, nonlocal processes radiated from (or to) the remote region, and dissipation processes (Gill et al. 1974; Pedlosky 1987; Garnier and Schopp 1999; Stammer and Wunsch 1999; Zhai et al. 2008; Yang et al. 2013; Kang et al. 2016). Early stochastic modeling studies provided evidences of direct wind-forced eddies in regions of weak currents (Frankignoul and Müller 1979; Müller and Frankignoul 1981), whereas local wind stress forcing is found not well correlated with the eddy activity in the vicinity of strong currents (White and Heywood 1995). In fact, a variety of observational studies have focused on the covariance between the Kuroshio Extension indices and atmospheric variables, all suggesting that the ocean-to-atmosphere forcing dominate the atmosphere-to-ocean forcing in this region, especially on the decadal time scale (Nonaka and Xie 2003; Qiu et al. 2014; Seo et al. 2014; O'Reilly and Czaja 2015; Wang and Liu 2015).

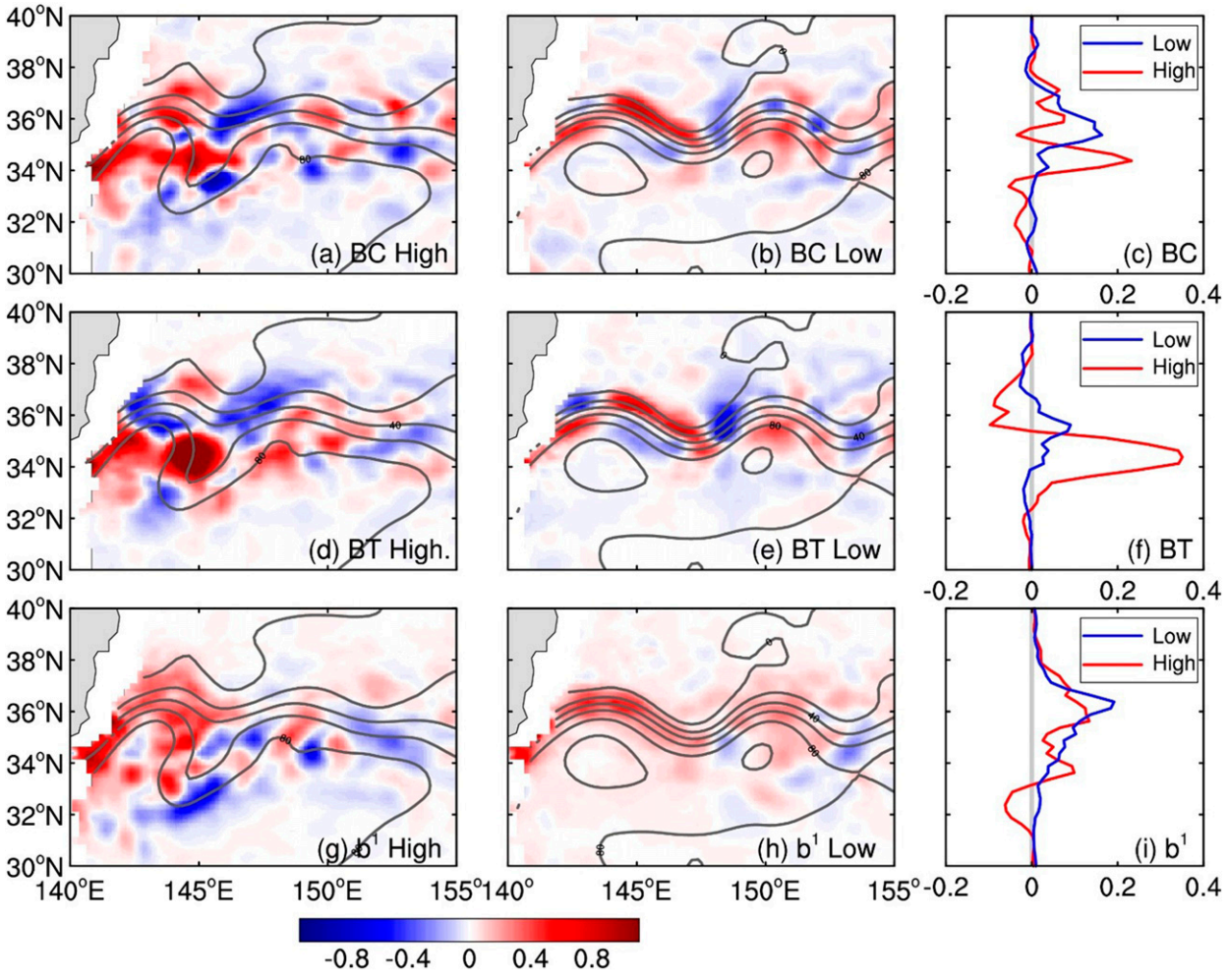

FIG. 6. Depth-averaged (upper 1000 m) BC maps (colored shading; 10^{-4} W m^{-3}) in the (a) high-EKE state and (b) low-EKE state and (c) zonal-mean structures from the ECCO2 state estimate. SSH composites (contours; cm) in each phase are superposed in (a) and (b). (d)–(f) As in (a)–(c), but for BT. (g)–(i) As in (a)–(c), but for b^1.

Considering this, we will only focus on the time-dependent barotropic and baroclinic instability processes and nonlocal energy advections and their relations with the decadal EKE variability; processes related to external forcings such as direct local wind forcing and flow–topography interactions and dissipation processes are not addressed in the present study.

a. Baroclinic and barotropic instabilities

Baroclinic and barotropic instabilities have been considered as the major energy sources for mesoscale eddies in the Kuroshio Extension (Hall 1991; Waterman et al. 2011; Yang and Liang 2016). In this subsection, we focus on the two instabilities, which are measured by the canonical baroclinic and barotropic transfer (see Liang 2016), respectively. The baroclinic transfer $\Gamma_A^{0\to1}$, when positive, is a measure of the energy transfer from MAPE to EAPE. Similarly, the barotropic transfer $\Gamma_K^{0\to1}$, when positive, is a measure of energy transfer from MKE to EKE. These two metrics are distinct from classical ones due to two reasons: first, they only involve processes among different scale windows and hence are essentially connected to instabilities in a generalized sense (Pedlosky 1987; Liang and Robinson 2007); second, they are time-dependent, four-dimensional field variables, thus providing the possibility to investigate the temporal variability of eddy–mean flow interactions and instabilities embedded in the complex dynamics of the decadally modulating Kuroshio Extension. For convenience, we will refer to the baroclinic and barotropic transfer as BC and BT, respectively.

In Figs. 6a and 6b, we show the horizontal maps of the depth-averaged (upper 1000 m) BC composites. The most noticeable feature is that BC is confined along the

narrow eastward jet in the low-EKE state, whereas it is spread out meridionally in the high-EKE state, which is in good agreement with the violent meanders in this state. Significant positive BC is found in the deep meander region, suggesting the active role played by standing meanders to elevate the regional baroclinic energy transfer. The latitudinal structure of the zonally averaged BC across the upstream Kuroshio Extension is shown in Fig. 6c. On average, BC peaks positively along the mean path, indicating that the eddies extract APE from the mean flow. During the low-EKE state, BC peaks at $0.17 \times 10^{-4}\,\mathrm{W\,m^{-3}}$ at ~36°N. In contrast to the low-EKE state, BC reaches $0.24 \times 10^{-4}\,\mathrm{W\,m^{-3}}$ at ~34°N during the high-EKE state. The southward migration of the maximum BC from the low-EKE state to the high-EKE state is in agreement with the southward shift of the jet. Overall, the above results are consistent with previous study by Bishop (2013), who also found the unstable meanders during the high-EKE state transfer significant APE from the background flow to the eddies. During the high-EKE state, the eddies are also found transferring more APE back to the mean flow at several spots, such as 33.8°N, 146°E and 36°N, 147.5°E. In contrast, similar negative BC spots are not clearly distributed during the low-EKE state. Those negative BC centers may be related to recurring passages of cold-core rings during the high-EKE state, as suggested by Bishop (2013).

Figures 6d and 6e show the barotropic transfer composite maps in the high-EKE state and low-EKE state, respectively. We see that the horizontal pattern of BT bears some resemblance with that of BC, which also peaks positively in the deep meander region during the high-EKE state, whereas it is confined within the strong but narrow jet with much reduced amplitude in the low-EKE years. The latitudinal distribution of the zonally averaged BT clearly shows that the BT peaks at $0.35 \times 10^{-4}\,\mathrm{W\,m^{-3}}$ during the high-EKE state, nearly 4 times larger than that in the low-EKE state ($0.09 \times 10^{-4}\,\mathrm{W\,m^{-3}}$). Besides, by comparing Figs. 6c and 6f, we can see that the violent meanders in the high-EKE state induce energy transfer from the mean flow to the eddies mainly through barotropic instability.

The distribution of buoyancy conversion term b^1 is plotted in Figs. 6g and 6h. As indicated in (3) and (4), this term acts as a proxy connecting the EKE and EAPE. Notice that it is important to distinguish the aforementioned BC and b^1. As BC measures the cross-scale energy transfer between the MAPE reservoir and EAPE reservoir, b^1 represents the energy conversion between the EAPE reservoir and EKE reservoir. The b^1 term is an inseparable part of baroclinic production of EKE through MAPE → EAPE → EKE pathway. Although the baroclinic pathway has been recognized as the main mechanism to generate EKE in the global ocean (von Storch et al. 2012), it might not be necessarily responsible for the EKE variation at low frequencies because the two different stages may not be correlated on the decadal time scale. Indeed, the composite EAPE seems to be not efficiently converted to EKE during the high-EKE state (Fig. 6i). Significant negative centers are found around the southern tip of the meander trough as well as the downstream region east of 150°E. A closer look at the baroclinic pathway (MAPE → EAPE → EKE) and the barotropic energy pathway (MKE → EKE) reveals that there is an interesting seesaw relation between them (Figs. 6f,i). During the low-EKE state, the baroclinic pathway is the major energy source of the EKE reservoir for the entire upstream Kuroshio Extension, whereas in the high-EKE state, the barotropic energy pathway prevails and the baroclinic pathway is suppressed. A similar seesaw relation is also found in a recent modeling study (Chen et al. 2016), which needs to be verified in observation.

Figure 7 provides the vertical structure of the energetics during the two different states along the zonal band of the largest EKE variance. During the low-EKE state, both BC and b^1 peak at a narrow band surrounding the jet axis where the largest isopycnal slope is observed (Figs. 7b,d). In contrast, the largest BC is confined around the southern flank of the jet axis where the isopycnal slope is largely flat during the high-EKE state (Fig. 7a), indicating the nonzonal component of the convoluted jet is responsible for the large energy transfer from MAPE to EAPE in this period. Further, the EAPE gained from the MAPE reservoir is not efficiently converted to EKE by buoyancy conversion at this band (Fig. 7c), implying that the baroclinic pathway is not the dominant factor controlling the decadal EKE modulation. Figures 7e and 7f show the BT term during the two states. Again, we see that the broadening meandering jet induces significant energy transfer from MKE to EKE around the southern flank of the jet axis, despite the relatively weak jet compared to that in the low-EKE state. Strong negative values are also found on the north flank of the jet during the high-EKE state, suggesting that eddies are frequently transferring KE back to the mean flow. This upscale cascade might be attributed to the existence of the north recirculation gyre (NRG), which has been recognized as an eddy-driven circulation in some recent studies (Qiu et al. 2008; Taguchi et al. 2010). Although embedded with negative values, the BT is overall positive, with a total transfer rate of 6.12 GW over the whole domain during the high-EKE state, in contrast to a rate of merely 0.69 GW in the low-EKE state. We may thus conclude that barotropic

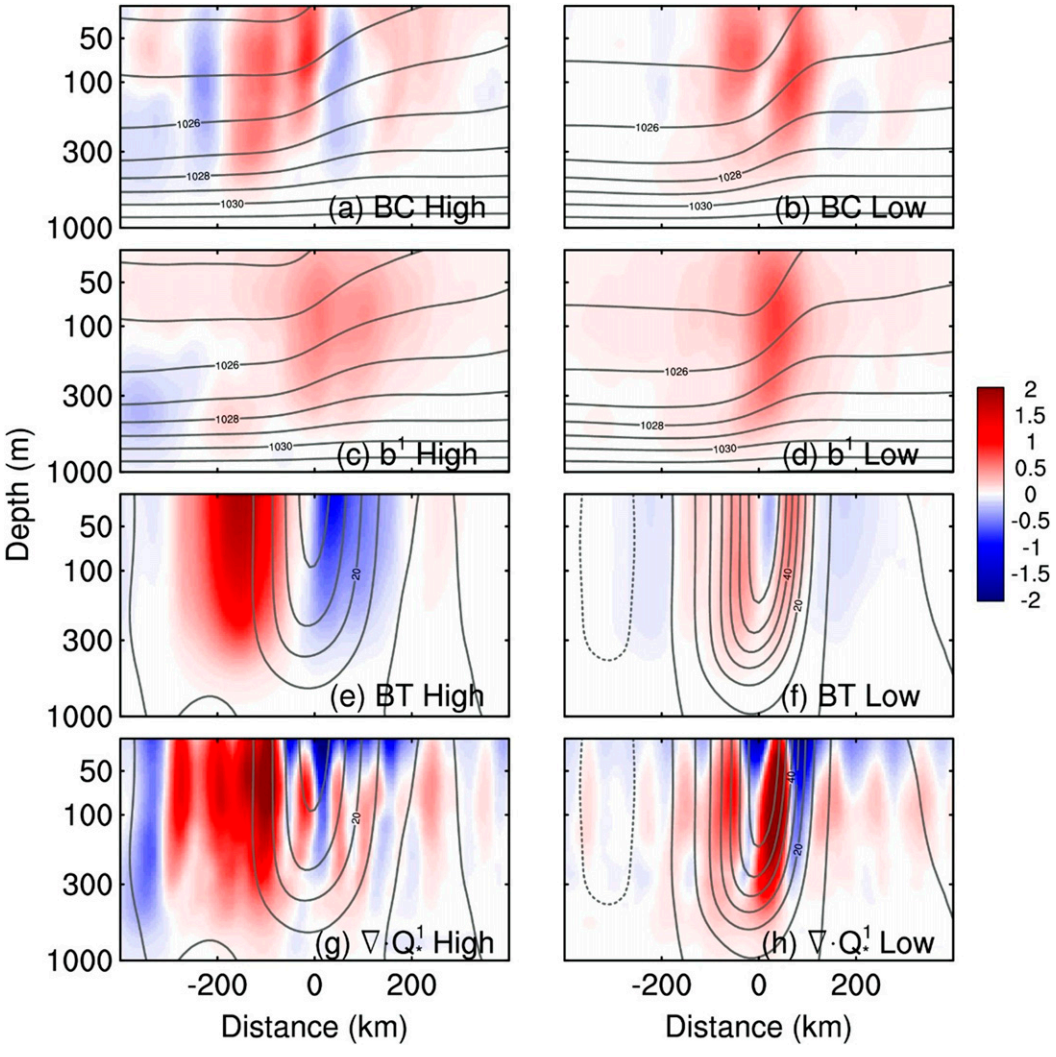

FIG. 7. Vertical sections of BC (colored shading, 10^{-4} W m^{-3}) and density (contours, kg m^{-3}) averaged between 142°–152°E in the (a) high-EKE state and (b) low-EKE state based on the ECCO2 state estimate. The x axis is the distance from the axis of Kuroshio Extension jet, which is defined by the latitude of the steepest SSH gradient (Delman et al. 2015). (c),(d) As in (a) and (b), but for b^1. (e),(f) As in (a) and (b), but for BT (color shades; 10^{-4} W m^{-3}) and zonal velocity (contours, cm s^{-1}). (g),(h) As in (e) and (f), but for $\nabla \cdot \mathbf{Q}^1_*$.

instability is the dominant mechanism that produces the decadal EKE modulation in the upstream Kuroshio Extension.

b. *Nonlocal energy transport*

Recent energetics studies have pointed out the nonlocal nature of eddy energy in the ocean (Grooms et al. 2013). In other words, nonlocal processes due to advection and pressure work might also weigh significantly in the local eddy energy budget. These terms appear in a divergence form in the energy budget equations and thus have zero global values but nonzero local values. In the MS-EVA formalism, the $\nabla \cdot \mathbf{Q}^1_K$ and $\nabla \cdot \mathbf{Q}^1_P$ terms are such nonlocal processes responsible for the EKE budget. In the following, we examine the combined effect of these two nonlocal terms (denoted as $\nabla \cdot \mathbf{Q}^1_*$). In our case, one may argue that the weakening in eddy activity when the jet is strong (i.e., in the low-EKE state) might be attributed to excessive energy advection out of the upstream Kuroshio Extension by strong eastward flow. In fact, this assertion has been used to explain the so-called midwinter minimum (MWM) phenomenon of the Pacific storm track (Chang 2001; Nakamura et al. 2002). To explore whether similar processes also happen in the upstream Kuroshio Extension, the vertical section of $\nabla \cdot \mathbf{Q}^1_*$ is shown in Figs. 7g and 7h. It is seen that this nonlocal term is almost

positively correlated to the BT term; the energy transporting out of the region is stronger in the high-EKE state than that in the low-EKE state, not as expected as that in the MWM case. Thus, we can safely conclude that the nonlocal energy advection is not responsible for the decadal EKE variation in this region.

c. *Temporal evolution*

To clarify how the regional EKE modulates with the barotropic instability, the area-averaged EKE and BT over the largest EKE variance region (see the rectangle box in Fig. 4b) is displayed in Fig. 8. Both time series are low-pass filtered to highlight the interannual-to-decadal variabilities. The EKE time series exhibits nearly simultaneous positive correlation ($r = 0.64$) with the BT, which is statistically significant at the 95% confidence level (critical value $r_0 = 0.45$) by the Student's t test. The number of degrees of freedom for the low-pass filtered EKE time series is estimated at 17 from its decorrelation time scale. The low-pass time series of area-averaged BC, b^1, and $\nabla \cdot \mathbf{Q}^1_*$ are also plotted in Fig. 8. The figure shows the BC is not significantly correlated with the EKE ($r = 0.31$ when BC leads EKE by ~5 months), and the buoyancy conversion is negatively correlated with EKE ($r = -0.32$ with no apparent phase lag), indicating that the baroclinic pathway breaks down at low frequencies due to insignificant phase correlations between BC and b^1. In addition, the nonlocal term $\nabla \cdot \mathbf{Q}^1_*$ and EKE are found positively correlated with a synchronous correlation coefficient of 0.55, indicating that the more EKE is generated, the more is being carried away from this region. To make sure the EKE generated through barotropic instability is accumulated within the upstream box, we plot the area-averaged BT $- \nabla \cdot \mathbf{Q}^1_*$ time series in Fig. 8i. The figure shows a nearly simultaneous positive correlation coefficient of 0.46 (statistically significant at a 95% confidence level), demonstrating that the EKE generated by BT is indeed responsible for the decadal EKE variability in this region. To see whether the above energetics are well balanced in terms of the temporal change of EKE, we plot the residue F^1_K series in Fig. 8k, which includes all the external forcing and internal dissipation processes. This residue term appears to be smaller than the dominant BT term by one order of magnitude, consistent with previous studies (Delman et al. 2015). The negative sign, small magnitude (Fig. 8k), and phase lag (Fig. 8l) indicate that the dissipation of EKE is more important than the local external forcing in the Kuroshio Extension. Besides, the small amplitude also indicates that the EKE energetics are overall balanced.

The temporal energetics results shown above clearly demonstrate that the barotropic instability is the dominant process for the decadal EKE modulations detected in the upstream Kuroshio Extension. As is shown in section 4a, the enhanced nonzonal meandering plays an important role to induce enhanced barotropic instability. Notice that the explanation for the time–lag between the low-pass transfer rate (i.e., BT and BC) and EKE is not trivial because eddies with long lifespan may survive more than 1 year and leave their imprints on the regional EKE and eddy–mean flow interactions on interannual time scales (Chang and Oey 2014). The exact eddy growth rate due to barotropic and baroclinic instabilities should be carefully examined, and we leave that to future studies.

5. Summary and discussion

Using the outputs from a dynamically consistent global eddying state estimate, the localized multiscale energy and vorticity analysis [MS-EVA; Liang and Robinson 2005, 2007; a comprehensive development is referred to Liang (2016)] was employed to investigate the mechanism of the decadal EKE variability in the upstream Kuroshio Extension region. We first used a new functional analysis tool (MWT; Liang and Anderson 2007) to decompose the associated fields into a slow, modulating mean flow component and a transient eddy component, instead of simply separating them into a time mean and its deviation. In this way, the low-frequency variability of the background jet is largely retained in the mean flow window, which is essential to investigate the time-varying diagram of the eddy–mean flow interactions and instabilities underlying the decadally modulating Kuroshio Extension system. Besides, the orthogonality between the resulting scale windows allows for a faithful representation of the eddy energetics.

The resulting energy maps and temporal series all demonstrate that barotropic instability is the primary source for the decadal EKE variability. The meanders have been found responsible for the generation of EKE in the upstream region. When the jet is weak, the meander of the upstream Kuroshio Extension jet is strong, which enhances both the barotropic transfer from MKE to EKE and baroclinic transfer from MAPE to EAPE. However, strong EAPE gained from the MAPE reservoir through the baroclinic instability process does not lead to increased EKE due to insufficient in-phase conversion from EAPE to EKE. In contrast, the growing meander induces significant barotropic instability, which efficiently releases energy from MKE to EKE, resulting in increased eddy activities in the upstream as the Kuroshio Extension is in the high-EKE state. During the low-EKE state, both

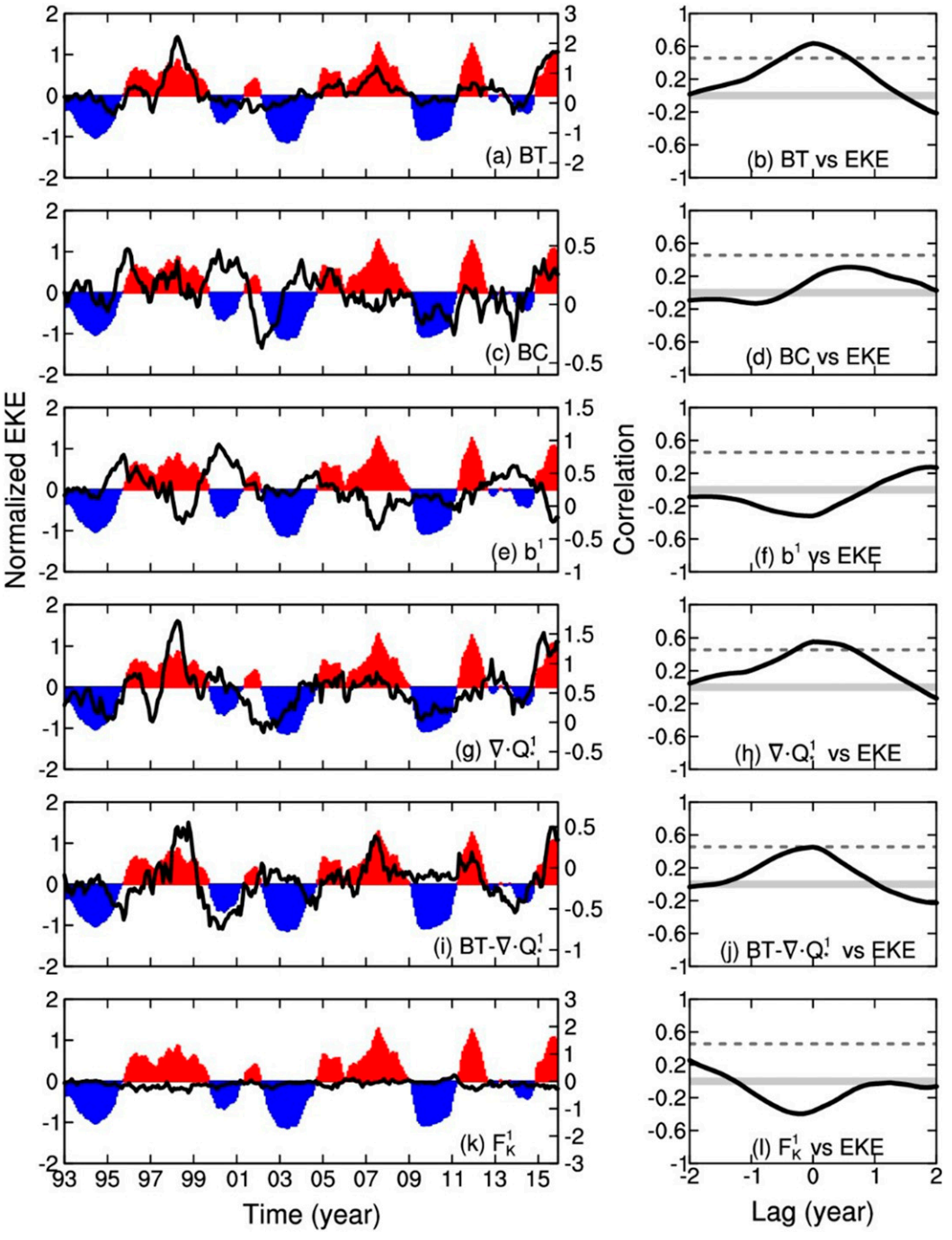

FIG. 8. (a) Time series of the normalized EKE (red and blue bars) and BT (black line; 10^{-4} W m^{-3}) averaged in the rectangular box in Fig. 4b based on the ECCO2 state estimate. Both times series are smoothed by applying a 1-yr running mean filter. (b) Lagged correlation between EKE and BT. A positive lag means that BT leads EKE. The dashed line indicates the 95% confidence level. (c),(d) As in (a) and (b), but for BC. (e),(f) As in (a) and (b), but for b^1. (g),(h) As in (a) and (b), but for $\nabla \cdot \mathbf{Q}^1_*$. (i),(j) As in (a) and (b), but for BT $- \nabla \cdot \mathbf{Q}^1_*$. (k),(l) As in (a) and (b), but for F^1_K.

BC and BT are found reduced in magnitude and confined along the narrow jet located farther north. In addition, the nonlocal energy advection exhibits a passively response to the low-frequency EKE variability, indicating the nonlocal process is not responsible for the decadal EKE modulation.

The above analysis has shed light on how the internal process, that is, barotropic instability, modulates the

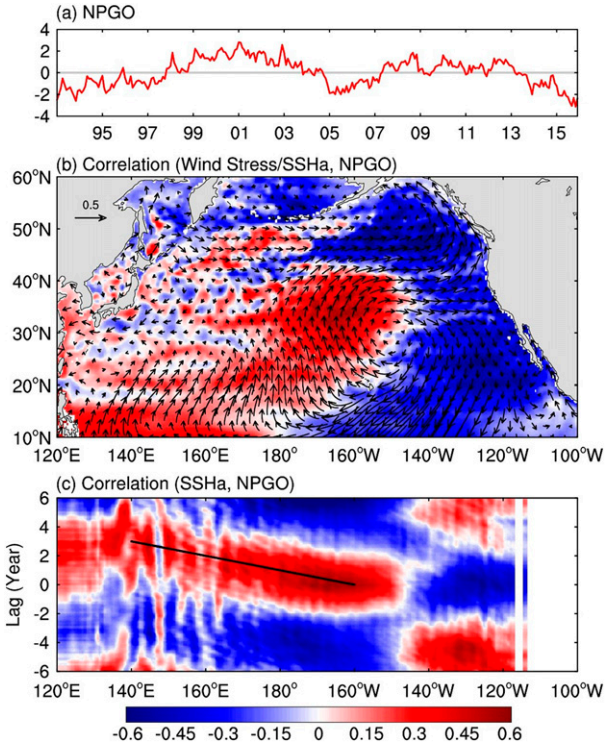

FIG. 9. (a) NPGO index. (b) Spatial correlation pattern between NPGO and surface wind stress from ECCO2 (vectors) and between NPGO and SSH anomaly from ECCO2 (colored shading) at 0-yr lag. (c) Time–longitude diagram of the lagged correlation between NPGO and SSH anomaly along the 31°–36°N band. A positive lag indicates that NPGO takes the lead. The annual cycle of the SSH anomaly is removed before processing the analysis.

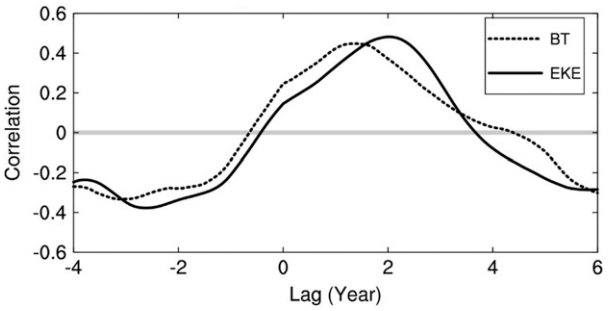

FIG. 10. Lagged correlation between the negative NPGO and the EKE time series (black) and between the negative NPGO and BT time series (dotted) integrated in the rectangle box in Fig. 4b. A positive lag indicates that NPGO takes the lead.

low-frequency EKE variation. It is natural to ask what mechanism might trigger such an internal oscillation. Is it externally forced or purely intrinsic? By analyzing the available sea surface height (SSH) data from the multiple satellite altimeters from 1993 to 2005, Qiu and Chen (2005) suggested that a meandering (straight) jet path of the Kuroshio Extension is induced by the southward (northward) migration of the inflow jet, which rides over a shallow (deep) segment of the Izu–Ogasawara Ridge. The southward (northward) migration of the jet is believed to be forced by the impinging negative (positive) SSH anomalies via the westward propagation of baroclinic Rossby waves generated in the central North Pacific (Qiu 2003; Ceballos et al. 2009; Nakano and Ishikawa 2010; Sasaki and Schneider 2011). Instead, some studies reported that changes in the meandering state of the Kuroshio Extension are related to the path of the Kuroshio south of Japan; a meandering (straight) jet path was associated with the Kuroshio taking the offshore nonlarge (nearshore nonlarge or typical large) meander path (Sugimoto and Hanawa 2012; Seo et al. 2014). As models have shown that the bimodality of the Kuroshio path south of Japan have a predominant intrinsic origin (Qiu and Miao 2000), Sugimoto and Hanawa (2012) argued that the meandering state of the Kuroshio Extension is not directly caused by the external Rossby waves.

Although no consensus has been reached so far, it is important to explore whether the aforementioned BT is related to the large-scale wind variability in the eastern basin. Previous studies have robust evidence of the Kuroshio Extension's response to the anomalous wind stress curl generated in the central North Pacific with a delay of a few years through westward propagation of baroclinic Rossby waves (Deser et al. 1999; Qiu 2003). Several recent studies have shown both the Pacific decadal oscillation (PDO) and the North Pacific Gyre Oscillation (NPGO) are good indicators for the decadal changes of Kuroshio Extension because the two modes are linearly correlated during the last two decades (Qiu and Chen 2010; Qiu et al. 2015). In the following, we choose the NPGO index to see whether it leaves any footprints in the internal dynamics underlying the Kuroshio Extension. The NPGO is an oceanic expression of the North Pacific Oscillation (NPO), defined by the PC-2 of SSH anomaly in the northeastern Pacific region 25°–62°N, 180°–110°W (Fig. 9a; Di Lorenzo et al. 2008; Ceballos et al. 2009). The spatial pattern of the NPGO reveals a clear dipole structure both in the projections of wind stress vector and SSH anomaly in the eastern and central North Pacific, as shown in Fig. 9b. Dynamically, the anomalous negative wind stress curl during the positive phase of NPGO over the subtropical gyre forces an anomalous positive SSH anomaly through local Ekman convergence. The wind-induced anomalous SSH signals then propagate westward into the upstream Kuroshio Extension after a delay of approximately 2 years, causing the regional SSH to change (Fig. 9c).

Figure 10 shows that the upstream BT is positively correlated with the negative NPGO index, with a correlation coefficient of 0.45 when the NPGO leads BT by ~2 yr. The above results indicate that the internal process that gives rise to the decadal EKE modulation in the upstream Kuroshio Extension is moderately correlated to the anomalous wind stress curl generated in the central North Pacific. Besides, the time lag also seems to be in agreement with the time period of the baroclinic adjustment in the North Pacific Ocean (Ceballos et al. 2009). Based on an eddy-resolving OGCM, Taguchi et al. (2007) suggested that the intrinsic nonlinear behavior of the Kuroshio Extension could be possibly excited by the externally generated baroclinic Rossby waves, but they did not provide a dynamical explanation. Using a simple shallow-water model, Pierini (2014) also showed a case of intrinsic variability in an excitable dynamical system triggered by the North Pacific Oscillation forcing. Consistent with Taguchi et al. (2007) and Pierini (2014), our preliminary results also suggest that an important fraction of the internal barotropic instability is forced and deterministic in nature. Nevertheless, a complete story is by no means an easy task in the Kuroshio Extension due to the varying external and internal forcings, and the potential nonlinear interplay between the two. Remote atmospheric forcing, the upstream Kuroshio inflow, the underlying bathymetry, and frontal nonlinear processes all need to be taken into account for a faithful understanding of the complex dynamics in this region. Further studies are needed to clarify how these individual processes as well as their mutual interactions might contribute to the decadal variability of the Kuroshio Extension and its associated eddies.

Acknowledgments. We appreciate Emanuele Di Lorenzo's important suggestions. Thanks are also due to an anonymous reviewer for his comments. Yang Yang thanks Andrew S. Delman for sharing the jet reference frame algorithm. The ECCO2 datasets are available from the site of the Jet Propulsion Laboratory, California Institute of Technology (http://ecco2.jpl.nasa.gov/), and the NPGO index is available online (at http://eros.eas.gatech.edu/npgo/data/NPGO.txt; the MS-EVA software is available at http://www.ncoads.org/). This work was supported by the National Science Foundation of China (NSFC) under Grant 41276032, by the Jiangsu Provincial Government through the Jiangsu Chair Professorship and the 2015 Jiangsu Program of Entrepreneurship and Innovation Group, and by the State Oceanic Administration through the National Program on Global Change and Air-Sea Interaction (GASI-IPOVAI-06). BQ and SC acknowledge support from NSF OCE-0926594.

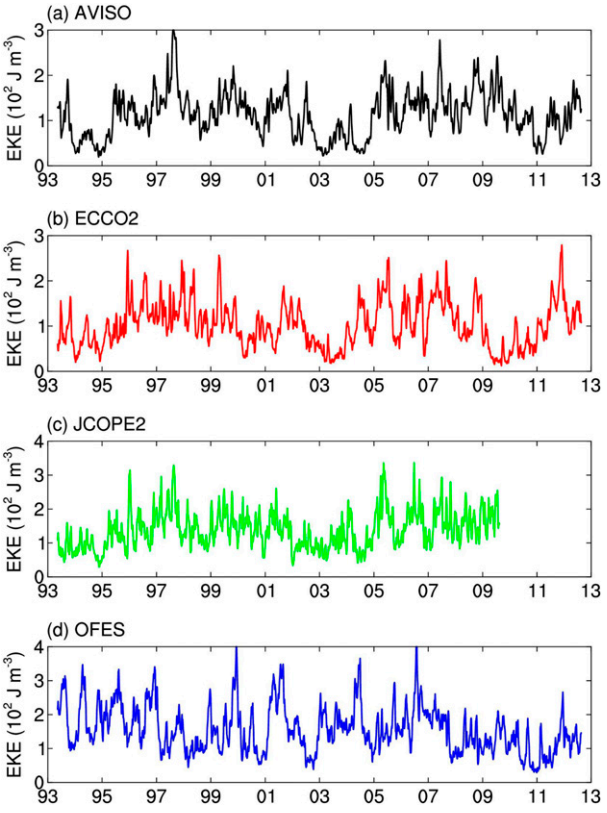

FIG. A1. Area-mean surface EKE time series (averaged over the rectangle box in Fig. 4b) constructed from (a) the satellite observation (AVISO), (b) the ECCO2 state estimate, (c) the JCOPE2 reanalysis, and (d) the OFES hindcast.

APPENDIX

Justification for the Dataset Selection

Area-mean (within the gray box in Fig. 4b) surface EKE density series from three different model outputs, namely, the ECCO2 state estimate, Japan Coastal Ocean Predictability Experiment 2 (JCOPE2) reanalysis, and the OGCM for the Earth Simulator (OFES) hindcast are shown here to see to what degree these modeling products fit in for our purpose in terms of the reproducibility of the decadal EKE variability in the Kuroshio Extension region.

The OFES is based on the Modular Ocean Model, version 3 (MOM3) with no observational data assimilated (Masumoto et al. 2004). Although several previous studies reported that the OFES data successfully reproduced the decadal SSH variability observed by satellite observations (Taguchi et al. 2007; Ceballos et al. 2009), the regional EKE level is largely biased (Fig. A1d; Table A1). Based on the Princeton Ocean Model (POM) and combined with the 3D variational

TABLE A1. Different datasets and the correlation between the area-mean EKE time series from these datasets and that from the satellite observation (AVISO).

Dataset	Optimization method	Correlation with AVISO series
ECCO2	Green function method (Menemenlis et al. 2005); no data taken in during forward run	0.64
JCOPE2	3D variational data assimilation (Miyazawa et al. 2009)	0.93
OFES	No data assimilated	−0.20

method to assimilate satellite observations and temperature–salinity profiles, the JCOPE2 reanalysis (Miyazawa et al. 2009) reproduced the observed EKE variability to a high degree (Fig. A1c; Table A1). The data assimilation is performed every 7 days to bring the model ''on track'' by minimizing the misfit between the model and the observation. Such an assimilation scheme will inevitably introduce jumps and unphysical sources/sinks that no longer satisfy the model equations (Wunsch et al. 2009). Thus, the model output may not be dynamically consistent and therefore may not be appropriate for eddy energetics analysis. In contrast, the ECCO2 state estimate is optimized by the observation by using a Green's function approach (Menemenlis et al. 2005). A least squares fit is employed for a number of control parameters of the model, for example, the initial temperature and salinity conditions, atmospheric surface boundary conditions, background vertical diffusivity, bottom drag, vertical viscosity, and so on (Wunsch et al. 2009). With these optimized control parameters, the model is run forward freely, just as in any ordinary model simulation. Since no data are taken in to interrupt the forward run, the state estimate is dynamically and kinematically consistent, without introducing nonphysical jumps and artificial imbalances in the numerical solution (Wunsch et al. 2009). To further check whether

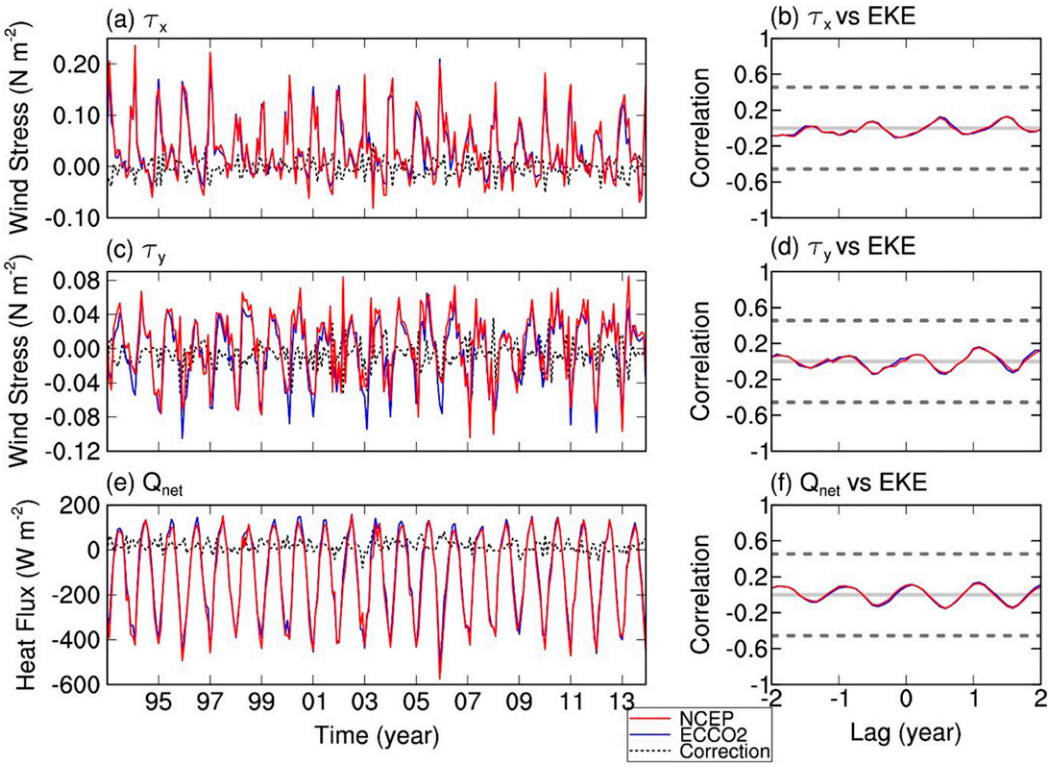

FIG. A2. (a) Monthly time series of the zonal wind stress from the NCEP reanalysis (red) and the ECCO2 state estimate (blue) averaged over the rectangle box in Fig. 4b. The dotted line denotes the difference between the two datasets. (b) Lagged correlation between the zonal wind stress from the NCEP reanalysis and the EKE time series (red line) and between the zonal wind stress from the ECCO2 state estimate and the EKE time series (blue line). A positive lag indicates that the zonal wind stress takes lead. The dashed lines indicate the 95% confidence level. (c),(d) As in (a) and (b), but for the meridional wind stress. (e),(f) As in (a) and (b), but for the surface heat flux.

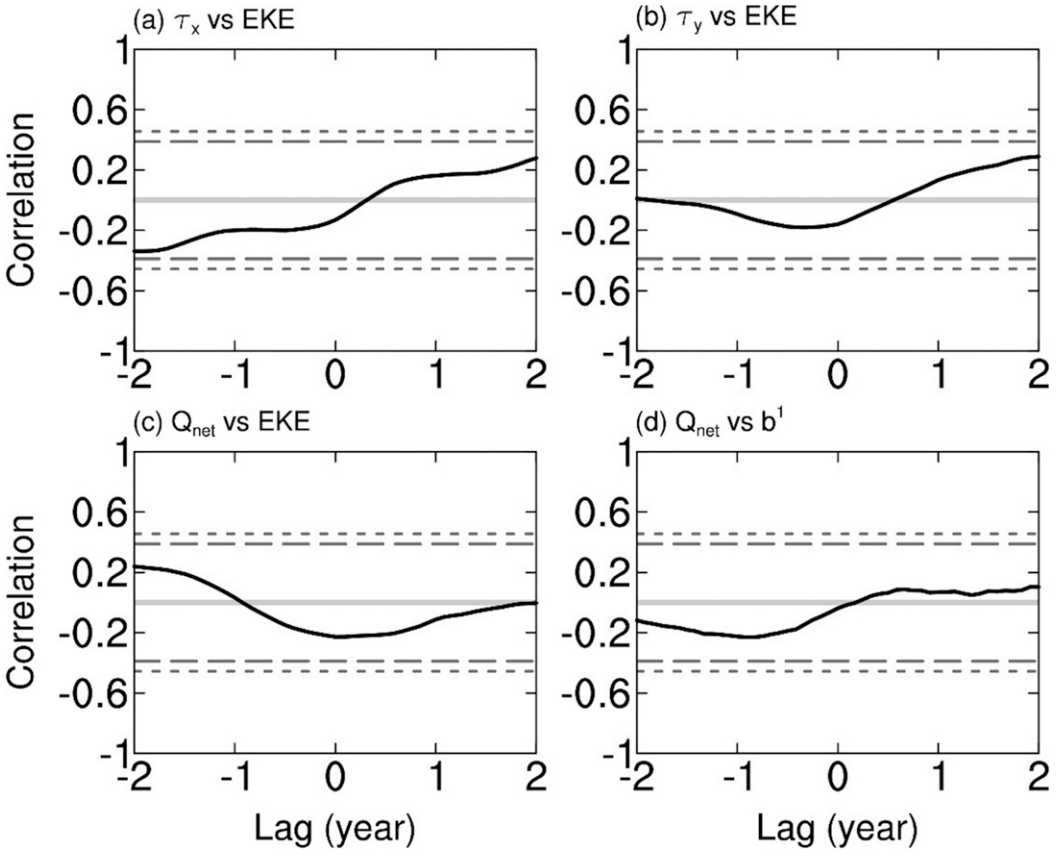

FIG. A3. (a) Lagged correlation between the corrected zonal wind stress averaged over the rectangle box in Fig. 4b and the EKE time series. All times series are smoothed by applying a 1-yr running mean filter. A positive lag indicates that the wind stress takes the lead. (b) As in (a), but for the meridional wind stress. (c) As in (a), but for the net heat flux. (d) The lagged correlation between the net heat flux and the buoyancy conversion. The long (short) dashed lines indicate the 90% (95%) confidence level.

the corrected surface boundary conditions (one of the control parameters) in the ECCO2 state estimates could impact the overall energetics, we plot the correlations between the EKE and ECCO2 as well as the NCEP surface fluxes averaged over our research box in Fig. A2. Although there exist noticeable differences (Figs. A2a,c,e), the correlations between the corrected surface fluxes and the model EKE are almost identical to the ones between the NCEP fluxes and the EKE (see the lead–lag correlations in Figs. A2b,d,f). Besides, the correlations between the local atmosphere forcings and the regional EKE are small, and, actually, they are far below significant. To see whether these surface fluxes and the EKE are correlated on the interannual-to-decadal time scale, we also plot the lead–lag correlations between the corresponding low-pass time series in Figs. A3a–c. Again, neither the wind stress nor the heat flux is significantly correlated with the associated EKE. (They are not statistically significant at both the 90% and 95% confidence level.) In fact, in this region, it is the ocean-to-atmosphere forcing that dominates the air–sea interaction, as reported previously (e.g., Nonaka and Xie 2003; Qiu et al. 2014; Seo et al. 2014). Here, the local heat flux is weakly and negatively correlated with the EKE ($r = -0.22$), which is consistent with previous findings that during the high-EKE state, the upper ocean releases more heat to the overlying atmosphere due to strengthened activities of the anticyclonic (warm) eddies detached from the Kuroshio Extension (Sugimoto and Hanawa 2011). To further check whether the corrected heat flux would impact the regional eddy activity through baroclinic instability processes, we plot the correlation between the heat flux and the buoyancy conversion term b^1 (i.e., EAPE $\rightarrow$ EKE) in Fig. A3d. Again, the lead–lag correlations are not significant. Moreover, these two processes are not correlated at lag 0, implying that the surface buoyancy forcing has no direct contributions to the generation of EKE at this region. The above results indicate that the assimilation scheme employed in the ECCO2 state estimate is not

likely to significantly affect the modeled EKE by correcting the local atmosphere forcings. Thus, we can safely conclude that the ECCO2 solution is appropriate for the diagnosis of ocean budgets. Figure A1b shows the area-mean EKE of the upstream Kuroshio Extension from the ECCO2 output. Obviously, the ECCO2 properly reproduced the two complete cycles of the decadal EKE variability in the upstream Kuroshio Extension region. For all the above reasons, we choose the ECCO2 state estimate as the input of the time-varying MS-EVA application, even though the correlation between ECCO2 and the satellite data is not as high as that between the JCOPE2 reanalysis and the satellite data (Table A1).

REFERENCES

Abernathey, R., and P. Cessi, 2014: Topographic enhancement of eddy efficiency in baroclinic equilibration. *J. Phys. Oceanogr.*, **44**, 2107–2126, doi:10.1175/JPO-D-14-0014.1.

Berloff, P., A. M. C. Hogg, and W. Dewar, 2007: The turbulent oscillator: A mechanism of low-frequency variability of the wind-driven ocean gyres. *J. Phys. Oceanogr.*, **37**, 2363–2386, doi:10.1175/JPO3118.1.

Bischoff, T., and A. F. Thompson, 2014: Configuration of a Southern Ocean storm track. *J. Phys. Oceanogr.*, **44**, 3072–3078, doi:10.1175/JPO-D-14-0062.1.

Bishop, S. P., 2013: Divergent eddy heat fluxes in the Kuroshio Extension at 144°–148°E. Part II: Spatiotemporal variability. *J. Phys. Oceanogr.*, **43**, 2416–2431, doi:10.1175/JPO-D-13-061.1.

Cai, M., S. Yang, H. M. Van Den Dool, and V. E. Kousky, 2007: Dynamical implications of the orientation of atmospheric eddies: A local energetics perspective. *Tellus*, **59A**, 127–140, doi:10.1111/j.1600-0870.2006.00213.x.

Ceballos, L. I., E. Di Lorenzo, C. D. Hoyos, N. Schneider, and B. Taguchi, 2009: North Pacific Gyre Oscillation synchronizes climate fluctuations in the eastern and western boundary systems. *J. Climate*, **22**, 5163–5174, doi:10.1175/2009JCLI2848.1.

Chang, E. K. M., 2001: GCM and observational diagnoses of the seasonal and interannual variations of the Pacific storm track during the cool season. *J. Atmos. Sci.*, **58**, 1784–1800, doi:10.1175/1520-0469(2001)058<1784:GAODOT>2.0.CO;2.

Chang, Y.-L., and L.-Y. Oey, 2014: Instability of the North Pacific Subtropical Countercurrent. *J. Phys. Oceanogr.*, **44**, 818–833, doi:10.1175/JPO-D-13-0162.1.

Chapman, C. C., A. M. Hogg, A. E. Kiss, and S. R. Rintoul, 2015: The dynamics of Southern Ocean storm tracks. *J. Phys. Oceanogr.*, **45**, 884–903, doi:10.1175/JPO-D-14-0075.1.

Chen, R., A. F. Thompson, and G. R. Flierl, 2016: Time-dependent eddy-mean energy diagrams and their application to the ocean. *J. Phys. Oceanogr.*, **46**, 2827–2850, doi:10.1175/JPO-D-16-0012.1.

Chen, X., B. Qiu, S. Chen, Y. Qi, and Y. Du, 2015: Seasonal eddy kinetic energy modulations along the North Equatorial Countercurrent in the western Pacific. *J. Geophys. Res. Oceans*, **120**, 6351–6362, doi:10.1002/2015JC011054.

Chiba, S., E. Di Lorenzo, A. Davis, J. E. Keister, B. Taguchi, Y. Sasai, and H. Sugisaki, 2013: Large-scale climate control of zooplankton transport and biogeography in the Kuroshio-Oyashio Extension region. *Geophys. Res. Lett.*, **40**, 5182–5187, doi:10.1002/grl.50999.

Delman, A. S., J. L. McClean, J. Sprintall, L. D. Talley, E. Yulaeva, and S. R. Jayne, 2015: Effects of eddy vorticity forcing on the mean state of the Kuroshio Extension. *J. Phys. Oceanogr.*, **45**, 1356–1375, doi:10.1175/JPO-D-13-0259.1.

Deser, C., M. A. Alexander, and M. S. Timlin, 1999: Evidence for a wind-driven intensification of the Kuroshio Current Extension from the 1970s to the 1980s. *J. Climate*, **12**, 1697–1706, doi:10.1175/1520-0442(1999)012<1697:EFAWDI>2.0.CO;2.

Di Lorenzo, E., and Coauthors, 2008: North Pacific Gyre Oscillation links ocean climate and ecosystem change. *Geophys. Res. Lett.*, **35**, L08607, doi:10.1029/2007GL032838.

Ducet, N., P. Y. Le Traon, and G. Reverdin, 2000: Global high-resolution mapping of ocean circulation from TOPEX/Poseidon and ERS-1 and -2. *J. Geophys. Res.*, **105**, 19 477–19 498, doi:10.1029/2000JC900063.

Elipot, S., and L. M. Beal, 2015: Characteristics, energetics, and origins of Agulhas Current meanders and their limited influence on ring shedding. *J. Phys. Oceanogr.*, **45**, 2294–2314, doi:10.1175/JPO-D-14-0254.1.

Ferrari, R., and C. Wunsch, 2009: Ocean circulation kinetic energy: Reservoirs, sources, and sinks. *Annu. Rev. Fluid Mech.*, **41**, 253–282, doi:10.1146/annurev.fluid.40.111406.102139.

Frankignoul, C., and P. Müller, 1979: Quasi-geostrophic response of an infinite β-plane ocean to stochastic forcing by the atmosphere. *J. Phys. Oceanogr.*, **9**, 104–127, doi:10.1175/1520-0485(1979)009<0104:QGROAI>2.0.CO;2.

Fu, L.-L., 2009: Pattern and velocity of propagation of the global ocean eddy variability. *J. Geophys. Res.*, **114**, C11017, doi:10.1029/2009JC005349.

Garnier, V., and R. Schopp, 1999: Wind influence on the mesoscale activity along the Gulf Stream and the North Atlantic currents. *J. Geophys. Res.*, **104**, 18 087–18 110, doi:10.1029/1999JC900070.

Gill, A. E., J. S. A. Green, and A. J. Simmons, 1974: Energy partition in the large-scale ocean circulation and the production of mid-ocean eddies. *Deep-Sea Res. Oceanogr. Abstr.*, **21**, 499–528, doi:10.1016/0011-7471(74)90010-2.

Grooms, I., L.-P. Nadeau, and K. S. Smith, 2013: Mesoscale eddy energy locality in an idealized ocean model. *J. Phys. Oceanogr.*, **43**, 1911–1923, doi:10.1175/JPO-D-13-036.1.

Hall, M. M., 1991: Energetics of the Kuroshio Extension at 35°N, 152°E. *J. Phys. Oceanogr.*, **21**, 958–975, doi:10.1175/1520-0485(1991)021<0958:EOTKEA>2.0.CO;2.

Hogg, A. M. C., P. D. Killworth, J. R. Blundell, and W. K. Dewar, 2005: Mechanisms of decadal variability of the wind-driven ocean circulation. *J. Phys. Oceanogr.*, **35**, 512–531, doi:10.1175/JPO2687.1.

Itoh, S., and I. Yasuda, 2010: Characteristics of mesoscale eddies in the Kuroshio–Oyashio Extension region detected from the distribution of the sea surface height anomaly. *J. Phys. Oceanogr.*, **40**, 1018–1034, doi:10.1175/2009JPO4265.1.

Jia, F., L. Wu, J. Lan, and B. Qiu, 2011: Interannual modulation of eddy kinetic energy in the southeast Indian Ocean by southern annular mode. *J. Geophys. Res.*, **116**, C02029, doi:10.1029/2010JC006699.

Kang, D., E. N. Curchitser, and A. Rosati, 2016: Seasonal variability of the Gulf Stream kinetic energy. *J. Phys. Oceanogr.*, **46**, 1189–1207, doi:10.1175/JPO-D-15-0235.1.

Kida, S., and Coauthors, 2015: Oceanic fronts and jets around Japan: A review. *J. Oceanogr.*, **71**, 469–497, doi:10.1007/s10872-015-0283-7.

Kwon, Y.-O., and C. Deser, 2007: North Pacific decadal variability in the Community Climate System Model version 2. *J. Climate*, **20**, 2416–2433, doi:10.1175/JCLI4103.1.

Latif, M., and T. P. Barnett, 1994: Causes of decadal climate variability over the North Pacific and North America. *Science*, **266**, 634–637, doi:10.1126/science.266.5185.634.

Liang, X. S., 2016: Canonical transfer and multiscale energetics for primitive and quasigeostrophic atmospheres. *J. Atmos. Sci.*, **73**, 4439–4468, doi:10.1175/JAS-D-16-0131.1.

——, and A. R. Robinson, 2005: Localized multiscale energy and vorticity analysis: I. Fundamentals. *Dyn. Atmos. Oceans*, **38**, 195–230, doi:10.1016/j.dynatmoce.2004.12.004.

——, and D. G. M. Anderson, 2007: Multiscale window transform. *Multiscale Model. Simul.*, **6**, 437–467, doi:10.1137/06066895X.

——, and A. R. Robinson, 2007: Localized multi-scale energy and vorticity analysis: II. Finite-amplitude instability theory and validation. *Dyn. Atmos. Oceans*, **44**, 51–76, doi:10.1016/j.dynatmoce.2007.04.001.

——, and ——, 2009: Multiscale processes and nonlinear dynamics of the circulation and upwelling events off Monterey Bay. *J. Phys. Oceanogr.*, **39**, 290–313, doi:10.1175/2008JPO3950.1.

Lorenz, E. N., 1955: Available potential energy and the maintenance of the general circulation. *Tellus*, **7**, 157–167, doi:10.3402/tellusa.v7i2.8796.

Marshall, J., A. Adcroft, C. Hill, L. Perelman, and C. Heisey, 1997: A finite-volume, incompressible Navier Stokes model for studies of the ocean on parallel computers. *J. Geophys. Res.*, **102**, 5753–5766, doi:10.1029/96JC02775.

Masumoto, Y., and Coauthors, 2004: A fifty-year eddy-resolving simulation of the world ocean: Preliminary outcomes of OFES (OGCM for the Earth Simulator). *J. Earth Simul.*, **1**, 35–56.

McCalpin, J. D., and D. B. Haidvogel, 1996: Phenomenology of the low-frequency variability in a reduced-gravity, quasigeostrophic double-gyre model. *J. Phys. Oceanogr.*, **26**, 739–752, doi:10.1175/1520-0485(1996)026<0739:POTLFV>2.0.CO;2.

Menemenlis, D., I. Fukumori, and T. Lee, 2005: Using Green's functions to calibrate an ocean general circulation model. *Mon. Wea. Rev.*, **133**, 1224–1240, doi:10.1175/MWR2912.1.

Miller, A. J., D. R. Cayan, and W. B. White, 1998: A westward-intensified decadal change in the North Pacific thermocline and gyre-scale circulation. *J. Climate*, **11**, 3112–3127, doi:10.1175/1520-0442(1998)011<3112:AWIDCI>2.0.CO;2.

——, F. Chai, S. Chiba, J. R. Moisan, and D. J. Neilson, 2004: Decadal-scale climate and ecosystem interactions in the North Pacific Ocean. *J. Oceanogr.*, **60**, 163–188, doi:10.1023/B:JOCE.0000038325.36306.95.

Miyazawa, Y., and Coauthors, 2009: Water mass variability in the western North Pacific detected in a 15-year eddy resolving ocean reanalysis. *J. Oceanogr.*, **65**, 737, doi:10.1007/s10872-009-0063-3.

Mizuno, K., and W. B. White, 1983: Annual and interannual variability in the Kuroshio Current System. *J. Phys. Oceanogr.*, **13**, 1847–1867, doi:10.1175/1520-0485(1983)013<1847:AAIVIT>2.0.CO;2.

Müller, P., and C. Frankignoul, 1981: Direct atmospheric forcing of geostrophic eddies. *J. Phys. Oceanogr.*, **11**, 287–308, doi:10.1175/1520-0485(1981)011<0287:DAFOGE>2.0.CO;2.

Nakamura, H., T. Izumi, and T. Sampe, 2002: Interannual and decadal modulations recently observed in the Pacific storm track activity and East Asian winter monsoon. *J. Climate*, **15**, 1855–1874, doi:10.1175/1520-0442(2002)015<1855:IADMRO>2.0.CO;2.

Nakano, H., and I. Ishikawa, 2010: Meridional shift of the Kuroshio Extension induced by response of recirculation gyre to decadal wind variations. *Deep-Sea Res. II*, **57**, 1111–1126, doi:10.1016/j.dsr2.2009.12.002.

Nishikawa, H., and I. Yasuda, 2011: Long-term variability of winter mixed layer depth and temperature along the Kuroshio jet in a high-resolution ocean general circulation model. *J. Oceanogr.*, **67**, 503–518, doi:10.1007/s10872-011-0053-0.

Nonaka, M., and S.-P. Xie, 2003: Covariations of sea surface temperature and wind over the Kuroshio and its extension: Evidence for ocean-to-atmosphere feedback. *J. Climate*, **16**, 1404–1413, doi:10.1175/1520-0442(2003)16<1404:COSSTA>2.0.CO;2.

——, H. Nakamura, Y. Tanimoto, T. Kagimoto, and H. Sasaki, 2006: Decadal variability in the Kuroshio–Oyashio Extension simulated in an eddy-resolving OGCM. *J. Climate*, **19**, 1970–1989, doi:10.1175/JCLI3793.1.

O'Reilly, C. H., and A. Czaja, 2015: The response of the Pacific storm track and atmospheric circulation to Kuroshio Extension variability. *Quart. J. Roy. Meteor. Soc.*, **141**, 52–66, doi:10.1002/qj.2334.

Pedlosky, J., 1987: *Geophysical Fluid Dynamics.* 2nd ed. Springer-Verlag, 710 pp.

Penduff, T., B. Barnier, W. K. Dewar, and J. J. O'Brien, 2004: Dynamical response of the oceanic eddy field to the North Atlantic Oscillation: A model–data comparison. *J. Phys. Oceanogr.*, **34**, 2615–2629, doi:10.1175/JPO2618.1.

Pierini, S., 2014: Kuroshio Extension bimodality and the North Pacific Oscillation: A case of intrinsic variability paced by external forcing. *J. Climate*, **27**, 448–454, doi:10.1175/JCLI-D-13-00306.1.

——, H. A. Dijkstra, and A. Riccio, 2009: A nonlinear theory of the Kuroshio Extension bimodality. *J. Phys. Oceanogr.*, **39**, 2212–2229, doi:10.1175/2009JPO4181.1.

Primeau, F., and D. Newman, 2008: Elongation and contraction of the western boundary current extension in a shallow-water model: A bifurcation analysis. *J. Phys. Oceanogr.*, **38**, 1469–1485, doi:10.1175/2007JPO3658.1.

Qiu, B., 2003: Kuroshio extension variability and forcing of the Pacific decadal oscillations: Responses and potential feedback. *J. Phys. Oceanogr.*, **33**, 2465–2482, doi:10.1175/2459.1.

——, and W. Miao, 2000: Kuroshio path variations south of Japan: Bimodality as a self-sustained internal oscillation. *J. Phys. Oceanogr.*, **30**, 2124–2137, doi:10.1175/1520-0485(2000)030<2124:KPVSOJ>2.0.CO;2.

——, and S. Chen, 2005: Variability of the Kuroshio Extension jet, recirculation gyre, and mesoscale eddies on decadal time scales. *J. Phys. Oceanogr.*, **35**, 2090–2103, doi:10.1175/JPO2807.1.

——, and ——, 2010: Eddy-mean flow interaction in the decadally modulating Kuroshio Extension system. *Deep-Sea Res. II*, **57**, 1098–1110, doi:10.1016/j.dsr2.2008.11.036.

——, and ——, 2013: Concurrent decadal mesoscale eddy modulations in the western North Pacific Subtropical Gyre. *J. Phys. Oceanogr.*, **43**, 344–358, doi:10.1175/JPO-D-12-0133.1.

——, ——, P. Hacker, N. G. Hogg, S. R. Jayne, and H. Sasaki, 2008: The Kuroshio Extension Northern Recirculation Gyre: Profiling float measurements and forcing mechanism. *J. Phys. Oceanogr.*, **38**, 1764–1779, doi:10.1175/2008JPO3921.1.

——, ——, N. Schneider, and B. Taguchi, 2014: A coupled decadal prediction of the dynamic state of the Kuroshio Extension system. *J. Climate*, **27**, 1751–1764, doi:10.1175/JCLI-D-13-00318.1.

——, ——, L. Wu, and S. Kida, 2015: Wind- versus eddy-forced regional sea level trends and variability in the North Pacific Ocean. *J. Climate*, **28**, 1561–1577, doi:10.1175/JCLI-D-14-00479.1.

Rhines, P., 1977: The dynamics of unsteady currents. *Marine Modeling*, E. D. Goldberg et al., Eds., The Sea—Ideas and Observations on Progress in the Study of the Seas, Vol. 6, John Wiley and Sons, 189–318.

Sasai, Y., K. J. Richards, A. Ishida, and H. Sasaki, 2010: Effects of cyclonic mesoscale eddies on the marine ecosystem in the Kuroshio Extension region using an eddy-resolving coupled physical-biological model. *Ocean Dyn.*, **60**, 693–704, doi:10.1007/s10236-010-0264-8.

Sasaki, Y. N., and N. Schneider, 2011: Decadal shifts of the Kuroshio Extension jet: Application of thin-jet theory. *J. Phys. Oceanogr.*, **41**, 979–993, doi:10.1175/2011JPO4550.1.

Schneider, N., A. J. Miller, and D. W. Pierce, 2002: Anatomy of North Pacific decadal variability. *J. Climate*, **15**, 586–605, doi:10.1175/1520-0442(2002)015<0586:AONPDV>2.0.CO;2.

Seager, R., Y. Kushnir, N. H. Naik, M. A. Cane, and J. Miller, 2001: Wind-driven shifts in the latitude of the Kuroshio–Oyashio Extension and generation of SST anomalies on decadal timescales. *J. Climate*, **14**, 4249–4265, doi:10.1175/1520-0442(2001)014<4249:WDSITL>2.0.CO;2.

Seo, Y., S. Sugimoto, and K. Hanawa, 2014: Long-term variations of the Kuroshio Extension path in winter: Meridional movement and path state change. *J. Climate*, **27**, 5929–5940, doi:10.1175/JCLI-D-13-00641.1.

Simonnet, E., and H. A. Dijkstra, 2002: Spontaneous generation of low-frequency modes of variability in the wind-driven ocean circulation. *J. Phys. Oceanogr.*, **32**, 1747–1762, doi:10.1175/1520-0485(2002)032<1747:SGOLFM>2.0.CO;2.

Smith, K. S., 2007: Eddy amplitudes in baroclinic turbulence driven by nonzonal mean flow: Shear dispersion of potential vorticity. *J. Phys. Oceanogr.*, **37**, 1037–1050, doi:10.1175/JPO3030.1.

Spall, M. A., 2000: Generation of strong mesoscale eddies by weak ocean gyres. *J. Mar. Res.*, **58**, 97–116, doi:10.1357/002224000321511214.

Stammer, D., and C. Wunsch, 1999: Temporal changes in eddy energy of the oceans. *Deep-Sea Res. II*, **46**, 77–108, doi:10.1016/S0967-0645(98)00106-4.

Sugimoto, S., and K. Hanawa, 2011: Roles of SST anomalies on the wintertime turbulent heat fluxes in the Kuroshio–Oyashio confluence region: Influences of warm eddies detached from the Kuroshio Extension. *J. Climate*, **24**, 6551–6561, doi:10.1175/2011JCLI4023.1.

——, and ——, 2012: Relationship between the path of the Kuroshio in the south of Japan and the path of the Kuroshio Extension in the east. *J. Oceanogr.*, **68**, 219–225, doi:10.1007/s10872-011-0089-1.

Sun, Z., Z. Zhang, W. Zhao, and J. Tian, 2016: Interannual modulation of eddy kinetic energy in the northeastern South China Sea as revealed by an eddy-resolving OGCM. *J. Geophys. Res. Oceans*, **121**, 3190–3201, doi:10.1002/2015JC011497.

Taguchi, B., S.-P. Xie, N. Schneider, M. Nonaka, H. Sasaki, and Y. Sasai, 2007: Decadal variability of the Kuroshio Extension: Observations and an eddy-resolving model hindcast. *J. Climate*, **20**, 2357–2377, doi:10.1175/JCLI4142.1.

——, B. Qiu, M. Nonaka, H. Sasaki, S.-P. Xie, and N. Schneider, 2010: Decadal variability of the Kuroshio Extension: Mesoscale eddies and recirculations. *Ocean Dyn.*, **60**, 673–691, doi:10.1007/s10236-010-0295-1.

Volkov, D. L., and L.-L. Fu, 2011: Interannual variability of the Azores Current strength and eddy energy in relation to atmospheric forcing. *J. Geophys. Res.*, **116**, C11011, doi:10.1029/2011JC007271.

von Storch, J.-S., C. Eden, I. Fast, H. Haak, D. Hernández-Deckers, E. Maier-Reimer, J. Marotzke, and D. Stammer, 2012: An estimate of the Lorenz energy cycle for the World Ocean based on the STORM/NCEP simulation. *J. Phys. Oceanogr.*, **42**, 2185–2205, doi:10.1175/JPO-D-12-079.1.

Wang, Y.-H., and W. T. Liu, 2015: Observational evidence of frontal-scale atmospheric responses to Kuroshio Extension variability. *J. Climate*, **28**, 9459–9472, doi:10.1175/JCLI-D-14-00829.1.

Waterman, S., N. G. Hogg, and S. R. Jayne, 2011: Eddy–mean flow interaction in the Kuroshio Extension region. *J. Phys. Oceanogr.*, **41**, 1182–1208, doi:10.1175/2010JPO4564.1.

White, M. A., and K. J. Heywood, 1995: Seasonal and interannual changes in the North Atlantic Subpolar Gyre from Geosat and TOPEX/POSEIDON altimetry. *J. Geophys. Res.*, **100**, 24 931–24 941, doi:10.1029/95JC02123.

Wunsch, C., P. Heimbach, R. Ponte, and I. Fukumori, 2009: The global general circulation of the ocean estimated by the ECCO-consortium. *Oceanography*, **22**, 88–103, doi:10.5670/oceanog.2009.41.

Yang, H., L. Wu, H. Liu, and Y. Yu, 2013: Eddy energy sources and sinks in the South China Sea. *J. Geophys. Res. Oceans*, **118**, 4716–4726, doi:10.1002/jgrc.20343.

Yang, Y., and X. S. Liang, 2016: The instabilities and multiscale energetics underlying the mean–interannual–eddy interactions in the Kuroshio Extension region. *J. Phys. Oceanogr.*, **46**, 1477–1494, doi:10.1175/JPO-D-15-0226.1.

Zemskova, V. E., B. L. White, and A. Scotti, 2015: Available potential energy and the general circulation: Partitioning wind, buoyancy forcing, and diapycnal mixing. *J. Phys. Oceanogr.*, **45**, 1510–1531, doi:10.1175/JPO-D-14-0043.1.

Zhai, X., R. J. Greatbatch, and J.-D. Kohlmann, 2008: On the seasonal variability of eddy kinetic energy in the Gulf Stream region. *Geophys. Res. Lett.*, **35**, L24609, doi:10.1029/2008GL036412.